REPORTRAPPORT

MAS

Modelling, Analysis and Simulation

Modelling, Analysis and Simulation

Oscillations in DC driven "barrier" discharges: numerical solutions, stability analysis and phase diagram

D.D. Šijačić, U.M. Ebert, I. Rafatov

REPORT MAS-E0424 DECEMBER 2004

CWI is the National Research Institute for Mathematics and Computer Science. It is sponsored by the Netherlands Organization for Scientific Research (NWO).
CWI is a founding member of ERCIM, the European Research Consortium for Informatics and Mathematics.

CWI's research has a theme-oriented structure and is grouped into four clusters. Listed below are the names of the clusters and in parentheses their acronyms.

Probability, Networks and Algorithms (PNA)

Software Engineering (SEN)

Modelling, Analysis and Simulation (MAS)

Information Systems (INS)

Oscillations in DC driven "barrier" discharges: numerical solutions, stability analysis and phase diagram

ABSTRACT

A short gas discharge layer sandwiched with a semiconductor layer between planar electrodes shows a variety of spatio-temporal patterns. The paper focusses on the spatially homogeneous spontaneous oscillations while a DC voltage is applied; the results on these homogeneous oscillations apply equally to a planar discharge in series with any resistor with capacitance. We define the minimal model, identify its independent dimensionless parameters and then present results of the full time-dependent numerical solutions of the model as well as of a linear stability analysis of the stationary state. Full numerical solutions and the results of the stability analysis agree very well. The stability analysis is then used for calculating bifurcation diagrams. We find semi-quantitative agreement with experiment for the diagram of bifurcations from stationary to oscillating solutions as well as for amplitude and frequency of the developing limit cycle oscillations.

Oscillations in DC driven "barrier" discharges: numerical solutions, stability analysis and phase diagram

Danijela D. Šijačić[1], Ute Ebert[1,2] and Ismail Rafatov[1,3,4]

[1] CWI, P.O.Box 94079, 1090 GB Amsterdam, The Netherlands,

[2] Dept. Physics, Eindhoven Univ. Techn., The Netherlands,

[3] American University – Central Asia, Bishkek, Kyrgyzstan and

[4] Middle East Technical University, Ankara, Turkey

(Dated: December 14, 2004)

A short gas discharge layer sandwiched with a semiconductor layer between planar electrodes shows a variety of spatio-temporal patterns. The paper focusses on the spatially homogeneous spontaneous oscillations while a DC voltage is applied; the results on these homogeneous oscillations apply equally to a planar discharge in series with any resistor with capacitance. We define the minimal model, identify its independent dimensionless parameters and then present results of the full time-dependent numerical solutions of the model as well as of a linear stability analysis of the stationary state. Full numerical solutions and the results of the stability analysis agree very well. The stability analysis is then used for calculating bifurcation diagrams. We find semi-quantitative agreement with experiment for the diagram of bifurcations from stationary to oscillating solutions as well as for amplitude and frequency of the developing limit cycle oscillations.

I. INTRODUCTION

Gas discharges on the transition from Townsend to glow regime exhibit a wealth of spatio-temporal structures. Besides striations, i.e., longitudinal waves in a long discharge column [1–5], short discharges with wide lateral aspect ratio can also exhibit rich spatio-temporal structures in the transversal direction as reported by a number of authors [6–9]. This is even the case when the externally applied voltage is stationary and the gas is pure, as long as the system is sandwiched between planar electrodes and at least one Ohmic layer. An interesting sequence of experiments has been performed in Münster [10, 11] where the bifurcations between different spatio-temporal states in parameter space were investigated very systematically.

As in our previous paper [12], we focus in the present one on the purely temporal oscillations that occur in a spatially homogeneous mode. This focus has two reasons: first, understanding the temporal structures is a first systematic step towards understanding the full spatio-temporal structures; second, there are numerous observations of temporal oscillations in comparable parameter regimes [13–20]. For the oscillations, the setup need not contain an Ohmic layer as in [10, 11], a resistor with capacitance in the circuit will have the same effect on the gas discharge.

In the previous paper [12], we concentrated on the question whether a simple two-component reaction-diffusion model for current and voltage in the gas discharge layer would be sufficient to describe the oscillations. Such a model is suggested through similarities with patterns formed in a number of physical, chemical or biological systems like the Belousov-Zhabotinski reaction, Rayleigh-Benard convection, patterns in bacterial colonies, in Dictyostelium or in nerval tissue etc. However, the actual results of a realistic gas discharge model are in conflict with a simple two-component reaction diffusion approximation that neglects the height and subsequent memory of the system. This can be seen, in particular, from the occurence of a period doubling cascade as well as from analytical model reductions [12]. Similar period doubling cascades are observed experimentaly in [21–26].

In the present paper, we continue the analysis of the full gas discharge model, coupled to a high-Ohmic layer and driven by a stationary voltage. The focus is now on quantitative comparison with experiment, on a stability analysis and on the derivation of bifurcation diagram. The specific experiment to be analyzed was performed in nitrogen at 40 mbar within a gap of 0.5 or 1 mm wide while the semiconductor was a layer of 1.5 mm photosensitively doped GaAs. To the whole structure, voltages in the range of 500 to 800 V were applied. As in our previous papers [12, 27, 28], we restrict the analysis to the direction normal to the layers, hence assuming homogeneity in the transversal directions. The experimental system actually shows a transition from a homogeneous stationary to a homogeneous oscillating state, and the theory presented here reproduces essential features of these experiments. At the same time, the investigation serves as a gauge point for a later analysis of spatio-temporal patterns.

In detail, we define the model as a set of partial differential equations and perform a dimensional analysis in Section II. In Section III, first the physical parameters and the numerical details of solving the PDE's in time are given. Then qualitative and quantitative results of numerical solutions and experiments are discussed. In particular, the hysteresis between stationary and oscillating solutions is demonstrated numerically, amplitude and frequency of the limit cycle oscillations as a function of applied voltage and conductivity of the semiconductor are compared with experimental results, and the physical mechanism of the oscillation is discussed. In Section IV, it is explained how the stability analysis about a sta-

tionary solution of the complete system is performed. In Section V, the results of the stability analysis are presented. First a convincing agreement between numerical solutions of the full PDE's and the stability analysis results is found. Then the stability analysis is used to calculate bifurcation diagrams for the transition from stationary to oscillating states that are then compared with experiment. The paper concludes with Section VI.

II. THE MODEL

The experiment consists of two layers, a gas discharge and a semiconductor, sandwiched between two planar electrodes to which a DC voltage is applied. In this section, the equations are defined and a dimensional analysis is performed to identify the independent parameter combinations of the problem. This also serves to identify physical processes and time scales.

A. Gas discharge layer

In the gas discharge, two ionization mechanisms cooperate to maintain conductivity: the so-called α process of impact ionization in the bulk of the discharge, and the γ process of secondary emission at the cathode. The classical "fluid" approximation consists of continuity equations for electron density n_e and positive ion density n_+, coupled to the Poisson equation for the electric field E:

$$\partial_t\, n_e \;+\; \partial_r J_e \;=\; source\ , \tag{1}$$
$$\partial_t\, n_+ \;+\; \partial_r J_+ \;=\; source\ , \tag{2}$$
$$\partial_r E \;=\; \frac{\mathrm{e}}{\varepsilon_0}\,\left(n_+ - n_e\right)\ . \tag{3}$$

The spatial coordinate r is normal to the layers, and in the present paper, it is assumed that there are no variations in the transversal directions. The gas is assumed to be non-attaching, i.e., no negative ions are formed. Also photo-ionization, Ohmic heating, nonlocal interactions and diffusion are neglected in this simplest approximation. The particle current densities J_e and J_+ are approximated by a drift motion that is linear in the field

$$J_e = -n_e\,\mu_e\, E\ , \quad J_+ = n_+\,\mu_+\, E\ . \tag{4}$$

The source term on the right hand side of Eqs. (1) and (2) is approximated by impact ionization in the classical Townsend form

$$source = |n_e\mu_e E|\,\alpha_0\,\mathrm{e}^{-E_0/|E|}\ . \tag{5}$$

The one-dimensional approximation of Eqs. (1), (2) and (3) makes the total electric current $J(t)$ homogeneous

$$\epsilon_0\partial_t E(r,t) + \mathrm{e}J_e(r,t) + \mathrm{e}J_+(r,t) = J(t)\quad ,\quad \partial_r J(t) = 0. \tag{6}$$

This identity can be used to substitute J_e or J_+ by $J(t)$. In the present analysis, we will keep $n_e(r,t)$ and $E(r,t)$ as independent fields and express n_+ and J_+ by these fields and the total current $J(t)$.

The model is completed by boundary conditions on the electrode. At the anode which is located at $r = 0$, electrons are absorbed and ions are absent:

$$J_+(0,t) = 0 \quad \Longleftrightarrow \quad n_+(0,t) = 0\ . \tag{7}$$

At the cathode which is located at $r = d$, impacting ions can liberate electrons by secondary emission with rate γ:

$$|J_e(d,t)| = \gamma\,|J_+(d,t)| \quad \Longleftrightarrow \quad \mu_e\,n_e(d,t) = \gamma\mu_+ n_+(d,t)\ . \tag{8}$$

Note that consistenly with [12, 27], but in contrast with most other literature, the anode is on the left hand side at $r = 0$. This has the advantage that the electric field is positive, and sign mistakes when evaluating E or $|E|$ cannot occur.

Substantial densities of charged particles change the electric field according to (3), and the electric field determines drift and ionization rates of the particles according to Eqs. (1), (2), (4) and (5). Therefore the process is nonlinear as soon as space charges become relevant. It causes the well-known transition from the linear Townsend discharge to the nonlinear glow discharge.

B. Semiconductor layer and complete circuit

The semiconductor layer of thickness d_s is assumed to have a homogeneous and field independent conductivity σ_s and dielectricity constant ϵ_s:

$$J_s(t) = \sigma_s E_s(t)\ , \quad q = \epsilon_s\epsilon_0\,\partial_r E\ . \tag{9}$$

As there are no space charges in the bulk of the semiconductor, the electric field is homogeneous, and voltage and field are related through $U_s(t) = E_s(t)d_s$. The equation of charge conservation $\partial_t q + \partial_r J_s = 0$ in one dimension leads again to the homogeneity of the total current density $J(t)$

$$\epsilon_s\epsilon_0\partial_t E_s(t) + J_s(t) = J(t), \tag{10}$$

that is the same as in the gas discharge (6). Hence in macroscopic parameters, the semiconductor solves

$$C_s\partial_t U_s(t) + J_s(t) = J(t)\quad ,\quad U_s(t) = R_s J_s(t), \tag{11}$$
$$C_s = \frac{\epsilon_s\epsilon_0}{d_s} \quad , \quad R_s = \frac{d_s}{\sigma_s}. \tag{12}$$

where C_s is the capacitance per area.

According to (11), perturbations of $U_s(t)$ or $J_s(t)$ decay on the Maxwell time scale

$$T_s = C_s R_s = \frac{\epsilon_s\epsilon_0}{\sigma_s}. \tag{13}$$

This time scale is independent of the thickness of the semiconductor layer although it represents the time that the charge needs to cross it. The time scale of the experimentally observed oscillations is of the order of T_s, and therefore also approximately proportional to $1/\sigma_s$ as will be discussed in Section III.D.

Actually, for the present investigation of one-dimensional oscillations, the specific structure of a planar semiconductor layer is not required, but any serial component of the electric circuit with capacitance C_s and resistance R_s will support the same equation (11).

The total stationary voltage U_t over the complete system is

$$U_t = U(t) + U_s(t) \; , \quad U(t) = \int_0^d E(r,t)dr \; , \quad \partial_t U_t = 0. \tag{14}$$

According to (11) and (14), the dynamics of the voltage $U(t)$ on the gas discharge obeys the equation

$$T_s \partial_t U = U_t - U(t) - R_s J(t). \tag{15}$$

C. Dimensional analysis and system definition

The dimensional analysis is performed as previously in [12, 27–29]. We introduce the dimensionless coordinates and fields

$$z = \frac{r}{X_0} \; , \quad \tau = \frac{t}{t_0} \; , \quad \sigma(z,\tau) = \frac{n_e(r,t)}{n_0}, \tag{16}$$

$$\mathcal{E}(z,\tau) = \frac{E(r,t)}{E_0} \; , \quad \mathcal{U} = \frac{U}{E_0 X_0} \; , \quad j = \frac{J}{en_0 X_0/t_0},$$

measuring quantities in terms of the intrinsic parameters of the system

$$X_0 = \frac{1}{\alpha_0} \; , \quad t_0 = \frac{1}{\alpha_0 \mu_e E_0} \; , \quad n_0 = \frac{\epsilon_0 \alpha_0 E_0}{e}. \tag{17}$$

After eliminating the ion dynamics by the total current $j(\tau)$, the equation of motion of the gas discharge becomes

$$\partial_\tau \sigma = \partial_z j_e + j_e \alpha(\mathcal{E}) \; , \quad j_e = \sigma \mathcal{E}, \tag{18}$$

$$\partial_\tau \mathcal{E} = j(\tau) - (1+\mu)j_e - \mu \mathcal{E} \partial_z \mathcal{E}, \tag{19}$$

and the boundary conditions (7) and (8) read

$$\partial_\tau \mathcal{E}(0,\tau) = j(\tau) - j_e(0,\tau), \tag{20}$$

$$\partial_\tau \mathcal{E}(L,\tau) = j(\tau) - \frac{1+\gamma}{\gamma} j_e(L,\tau). \tag{21}$$

The intrinsic dimensionless parameters of the gas discharge are the mobility ratio μ of electrons and ions and the length ratio L of system size and inverse cross section of impact ionization

$$\mu = \frac{\mu_+}{\mu_e} \; , \quad L = \frac{d}{X_0}. \tag{22}$$

The discharge is coupled to the semiconductor and the DC voltage source $\mathcal{U}_t$ through (11) as

$$\tau_s \partial_\tau \mathcal{U}(\tau) = \mathcal{U}_t - \mathcal{U}(\tau) - \mathcal{R}_s j(\tau), \tag{23}$$

with the dimensionless parameters

$$\tau_s = \frac{T_s}{t_0}. \quad , \quad \mathcal{R}_s = \frac{R_s}{E_0 t_0/(en_0)}. \tag{24}$$

The voltage $\mathcal{U}(\tau) = \int_0^L \mathcal{E}(z,\tau)\, dz$ is related to the electric field $\mathcal{E}$ and potential ϕ in differential form as

$$\mathcal{E}(z,\tau) = -\partial_z \phi(z,\tau) \; , \quad \mathcal{U}(\tau) = \phi(0,\tau) - \phi(L,\tau), \tag{25}$$

where gauge freedom allows one to choose

$$\phi(0,\tau) = 0. \tag{26}$$

Hence the dynamics of the complete system is described by Eqs. (18)–(21), (23), (25) and (26). The system is characterized completely by the independent dimensionless parameters μ, L and γ for the gas discharge layer, τ_s and $\mathcal{R}_s$ for the semiconductor layer and the total applied DC voltage $\mathcal{U}_t$.

III. NUMERICAL SOLUTIONS OF THE DYNAMICS

In this section, this dynamical model is solved numerically and the results are compared with experiments. We discuss physical parameters under A and numerical details under B. In C, qualitative features of experimental and numerical system are compared like the bistability between stationary and oscillating state. In D, a quantitative comparison between theory and experiment is performed, and the dependence of amplitude and frequency of the oscillation as a function of $\mathcal{U}_t$ and $1/\mathcal{R}_s$ is determined numerically. Finally, in E, we discuss the mechanism of the oscillations and identify the surface charge effects that are inherent in our model.

A. Physical parameters

In the experiment [10], nitrogen at a pressure of 40 mbar was used in gaps with widths of 0.5 or 1 mm. The article [10] contains mainly data for the 0.5 mm gap, while the Ph.D. thesis [11] also contains more data for 1 mm. The gas discharge was coupled to a semiconductor layer of GaAs with a width of $d_s = 1.5$ mm and a dielectricity constant $\epsilon_s = 13.1$. Through photosensitive doping, the conductivity of the semiconductor layer could be increased by about an order of magnitude; the dark conductivity was $\sigma_s = 3.2 \cdot 10^{-8} (\Omega \text{cm})^{-1}$. For the discharge gap of 0.5 mm width, voltages in the range of 500 to 600 V were used; for the gap of 1 mm width, the applied voltages were in the range of 580 to 740 V.

Of course, the predictive power of the theory depends on the model approximations as well as on the chosen parameters. Our simple classical model will not give fully quantitative agreement. On the other hand, its simple structure and few parameters give a chance of physical understanding and control.

For the gas discharge, we used the ion mobility $\mu_+ = 23.33$ cm^2/Vs and electron mobility $\mu_e = 6666.6$ cm^2/Vs. For $\alpha_0 = Ap = [27.78\mu\text{m}]^{-1}$ and $E_0 = Bp = 10.26$ kV/cm, the value from [30] was used. The gap widths of $d = 0.5$ and 1 mm then correspond to dimensionless gap widths $L = 18$ and 36. For γ, we used the value 0.08 determined from experimental Paschen curves in [11]. It should be noted that our classical model predicts that the Paschen curves (i.e., the breakdown voltage U of the gas discharge as a function of pressure times gap width pd) for different system sizes should be indistinguishable. In practice, they do not precisely fall on top of each other.
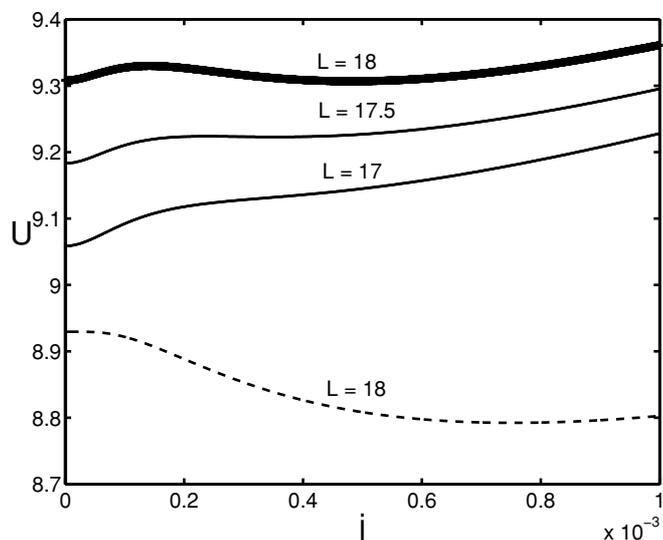
FIG. 1: Current-voltage characteristics for $\gamma = 0.08$ (solid lines) and $\gamma = 0.1$ (dashed line) for the dimensionless gap widths L as indicated in the figure.

It is interesting to note how sensitive the theoretical results are to small changes of the secondary emission coefficient γ, in particular, for the short gap with $L = 18$. This is illustrated in Fig. 1. The upper three solid lines show the shape of the current voltage characteristics for $\gamma = 0.08$ and gap widths of $L = 17$, 17.5 and 18. As discussed in more detail in [27, 28], the characteristics can be supercritical ($L = 17$, positive differential conductivity for all values of the current j), mixed II ($L = 17.5$, Townsend breakdown voltage lower than the local voltage minimum for $j \neq 0$) or mixed I ($L = 18$, Townsend breakdown voltage higher than the local voltage minimum for $j \neq 0$). The dashed line shows the characteristics for $L = 18$ and $\gamma = 0.1$. $\mathcal{U}$ then overall is considerably lower and the characteristics is fully subcritical, i.e., the

voltage has only one minimum as function of current j and this occurs for a value $j \neq 0$. This subcritical behavior corresponds to the classical textbook case where the characteristics bends down from the Townsend breakdown voltage towards a voltage minimum in the glow discharge regime — as we have discussed in [27, 28] in detail, this requires a sufficiently large system size. For $\gamma = 0.08$, the characteristics becomes subcritical for system size $L > L_{crit} = e^2 \ln\left[(1 + \gamma)/\gamma\right] = 19.2$ while the transition to supercritical behavior is determined numerically [27] to the value of $L = 17.2$.

Data on the coefficient γ of secondary electron emission are relatively scarce, so it is quite common [31] to use it as an adjustable parameter as we do. The tabulated data for $\alpha_0 = Ap$ and $E_0 = Bp$ from [30] together with the Paschen curve for $d = 0.5$ mm from [11] would suggest $\gamma = 0.03$, but that would mean that the characteristics would be supercritical up to $L = 24.9$, then it would develop some regime with negative differential conductivity, and it would become subcritical only for $L > L_{crit}(\gamma = 0.03) = 26.1$.

We conclude that the gap with width 0.5 mm (corresponding to $L = 18$) is so sensitive to the not very well known parameter γ that an analysis of the experimental data would be rather uncertain. Furthermore, the approximation of purely local interactions becomes worse in shorter gaps. Finally, the electric fields in short discharges are higher and vary more; therefore the assumption that γ does not depend on E becomes more restrictive. For this reason, we chose to analyze the system with gap width 1 mm ($L = 36$).

We recall that the following intrinsic scales

$$X_0 \approx 27.78 \; \mu\text{m} \quad , \quad t_0 \approx 40.6 \cdot 10^{-12} \text{ s},$$
$$n_0 \approx 2.04 \cdot 10^{12}/\text{cm}^3 \quad , \quad E_0 \approx 10.26 \, \text{kV/cm} \quad (27)$$

enter the dimensional analysis (16). Therefore the dimensionless parameters for a system with gap width of $d = 1$ mm and applied voltages in the range from 500 to 740 V are in our simulations:

$$\mu = 0.0035 \quad , \quad L = 36 \quad , \quad \gamma = 0.08,$$
$$\tau_s = 0.243 \, \mathcal{R}_s \quad , \quad 3 \cdot 10^5 \leq \mathcal{R}_s \leq 3 \cdot 10^6$$
$$17.5 \leq \mathcal{U}_t \leq 26. \quad (28)$$

Here, the dimensionless capacitance of the semiconductor layer is $\mathcal{C}_s = 0.243$, and its dimensionless characteristic time scale is $\tau_s = \mathcal{C}_s \mathcal{R}_s$. The value $\mathcal{R}_s = 3 \cdot 10^6$ for the semiconductor resistance corresponds to the dark conductivity of $\sigma_s = 3.2 \cdot 10^{-8}/(\Omega\text{cm})$, and $\mathcal{R}_s = 3 \cdot 10^5$ corresponds to the fully photo-activated conductivity $\sigma_s = 3.2 \cdot 10^{-7}/(\Omega\text{cm})$. The dimensionless voltage range of $17.5 \leq \mathcal{U}_t \leq 26$ corresponds to the dimensional range of $500 \text{ V} \leq U_t \leq 740 \text{ V}$.

B. Numerical solution strategy

Equations (18)–(26) were solved numerically with an implicit temporal discretization, which makes the calculation numerically stable for arbitrary time and space steps. After discretization, the dynamical equations (18) and (19) have the form

$$\frac{\sigma_i^{m+1} - \sigma_i^m}{\Delta\tau} = \frac{(\sigma\mathcal{E})_{i+1}^{m+1} - (\sigma\mathcal{E})_i^{m+1}}{\Delta z} + \left(\mathcal{E}\sigma\,\alpha(\mathcal{E})\right)_i^{m+1},$$

$$\frac{\mathcal{E}_i^{m+1} - \mathcal{E}_i^m}{\Delta\tau} = j^m - \mu\mathcal{E}_i^m\frac{\mathcal{E}_i^{m+1} - \mathcal{E}_{i-1}^{m+1}}{\Delta z} - (1+\mu)\,(\mathcal{E}\sigma)_i^m,$$
(29)

where i parametrizes the spatial and m the temporal grid.

For known σ^m and $\mathcal{E}^m$ at time step m, the boundary condition on the left (20) determines

$$\mathcal{E}_1^{m+1} = \mathcal{E}_1^m + \Delta\tau\left(j^m - (\mathcal{E}\sigma)_1^m\right), \qquad (30)$$

then the other fields $\mathcal{E}_i^{m+1}$ are calculated successively from the left to right $(i = 2, 3, .., N)$ by the equation

$$\mathcal{E}_i^{m+1} = \frac{\mathcal{E}_i^m\left(1 + \frac{\mu\Delta\tau}{\Delta z}\mathcal{E}_{i-1}^{m+1} - (1+\mu)\Delta\tau\sigma_i^m\right) + \Delta\tau j^m}{1 + \frac{\mu\Delta\tau}{\Delta z}\mathcal{E}_i^m}. \qquad (31)$$

For σ_i^{m+1}, the boundary condition on the right (21) determines

$$\sigma_N^{m+1} = \left(j^m - \frac{\mathcal{E}_N^{m+1} - \mathcal{E}_N^m}{\Delta\tau}\right) \Big/ \left(\frac{1+\gamma}{\gamma}\mathcal{E}_N^{m+1}\right). \qquad (32)$$

The remaining σ_i^{m+1} can now be calculated successively from the right to left $(i = N-1, N-2, .., 1)$ as

$$\sigma_i^{m+1} = \frac{\sigma_i^m + \frac{\Delta\tau}{\Delta z}(\sigma\mathcal{E})_{i+1}^{m+1}}{1 + \frac{\Delta\tau}{\Delta z}\mathcal{E}_i^{m+1} - \Delta\tau\mathcal{E}_i^{m+1}\alpha(\mathcal{E}_i^{m+1})}. \qquad (33)$$

The total current j^m in these equations is determined by

$$j^m = \frac{1}{\mathcal{R}_s + \tau_s L}\Bigg[\mathcal{U}_t - \mathcal{U}^m + \tau_s\left(\frac{\mu}{2}\left((\mathcal{E}_N^m)^2 - (\mathcal{E}_1^m)^2\right)\right.$$

$$\left.+ (1+\mu)\Delta z\sum_{i=1}^{N-1}(\mathcal{E}\sigma)_i^m\right)\Bigg]. \qquad (34)$$

This identity can be derived from (23) where $\partial_\tau\mathcal{U}$ is identified with $\int_0^L dz\,\partial_\tau\mathcal{E}$ through (25), and then for $\partial_\tau\mathcal{E}$, the identity (19) is used.

The results presented in Figures 2 to 9 are derived on a grid with $\Delta z = 36/600$ and $\Delta\tau = 180/600$ which gives a sufficient numerical accuracy.

C. Qualitative features of experimental and numerical oscillations: hysteresis amd limit cycles

The experiments [10] show approximately periodic oscillations. They are quite anharmonic with long phases of low current interrupted by a short current pulse. Depending on applied voltage $\mathcal{U}_t$ and resistance of the semiconductor layer $\mathcal{R}_s$, either the homogeneous stationary or the homogeneous oscillating state are dynamically stable. Inbetween, there is a regime of bistability where it depends hysteretically on the previous state whether the system is stationary or oscillating.

The same qualitative behavior can be observed in our numerical solutions. First, the upper panel in Fig. 2 shows the current $j(\tau)$ as a function of time for the system with the parameters from (28) and $\mathcal{R}_s = 4\cdot10^5$ and $\mathcal{U}_t = 19.5$ (which corresponds to $\sigma_s = 2.4\cdot10^{-7}/(\Omega\text{cm})$ and $U_t = 555$ V). After some transient, the current relaxes to periodic unharmonic oscillations. The lower panel in Fig. 2 shows the voltage $\mathcal{U}(\tau)$ over the gas discharge; the voltage on the semiconductor is correspondingly $\mathcal{U}_t - \mathcal{U}(\tau)$. In dimensional units, the peak current of the oscillations is about 9 mA/cm^2 and the frequency is about 120 kHz.
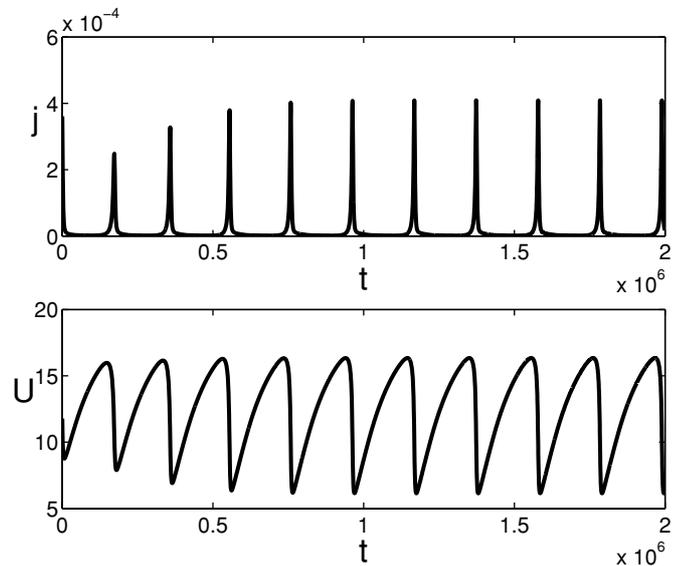
FIG. 2: $j(\tau)$ and $\mathcal{U}(\tau)$ for the parameters from (28), $\mathcal{R}_s = 4\cdot10^5$ and $\mathcal{U}_t = 19.5$.

The same numerical data for current j and voltage $\mathcal{U}$ are shown as a phase space plot in Fig. 3. The figure shows more precisely the approach to a limit cycle. Fig. 3 contains two additional lines, namely the current voltage characteristics of the gas discharge $\mathcal{U} = \mathcal{U}(j)$ and the load line $\mathcal{U} = \mathcal{U}_t - \mathcal{R}_s j$. Their intersection marks the stationary solution of the system. In the present case, it is located in the low current regime close to the Townsend limit, while the peak current explores the regime of subnormal glow.

The system of Figs. 2 and 3 is actually in the bistable regime. For different initial conditions that are a sufficiently small perturbation of the stationary state, the same system relaxes to the stationary point. This is shown as phase space plot in Fig. 4.
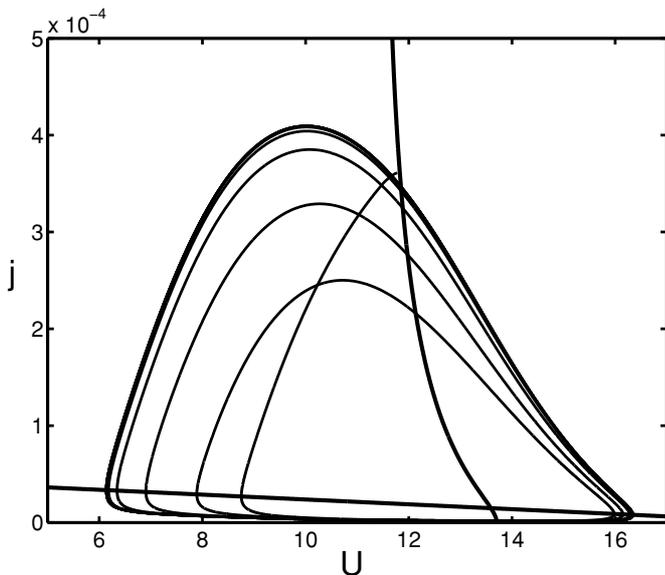
FIG. 3: Phase space plot of the data from Fig. 2. After some transient time, a stable limit cycle is reached. Also drawn are the current-voltage-characteristics $\mathcal{U} = \mathcal{U}(j)$ of the gas discharge and the load line $\mathcal{U} = \mathcal{U}_t - \mathcal{R}_s j$. Their intersection denotes the stationary solution.
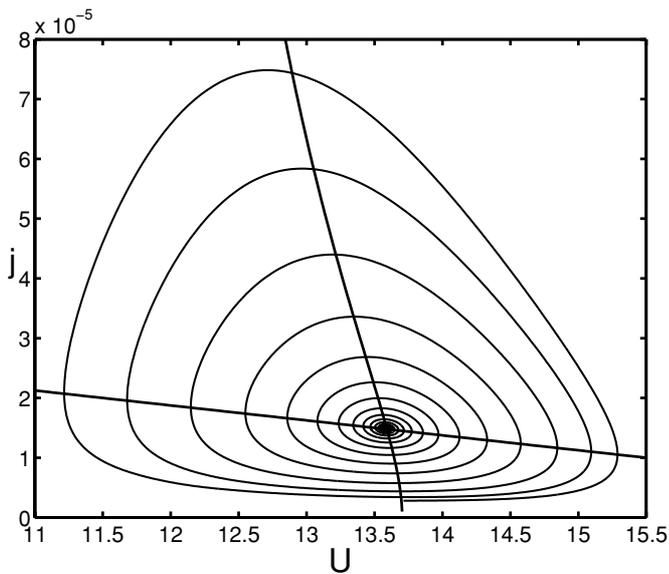
FIG. 4: System with exactly the same parameters as in Figs. 2 and 3, but for different initial conditions. The system now spirals inwards towards the stationary point.

If the applied voltage $\mathcal{U}_t$ becomes large enough, the stationary state becomes unstable for any initial condition. The search for appropriate parameters was guided by the stability analysis described in sections IV and V of this paper. We find that $\mathcal{U}_t = 24$ ($U_t = 684$ V) with all other parameters unchanged can be used as an example

of a system where the stationary solution is dynamically unstable, and the system runs away from this initial state and eventually reaches a limit cycle oscillation. This behavior is shown in Fig. 5 as $j(\tau)$ and $\mathcal{U}(\tau)$, while Fig. 6 shows the corresponding phase space plot.
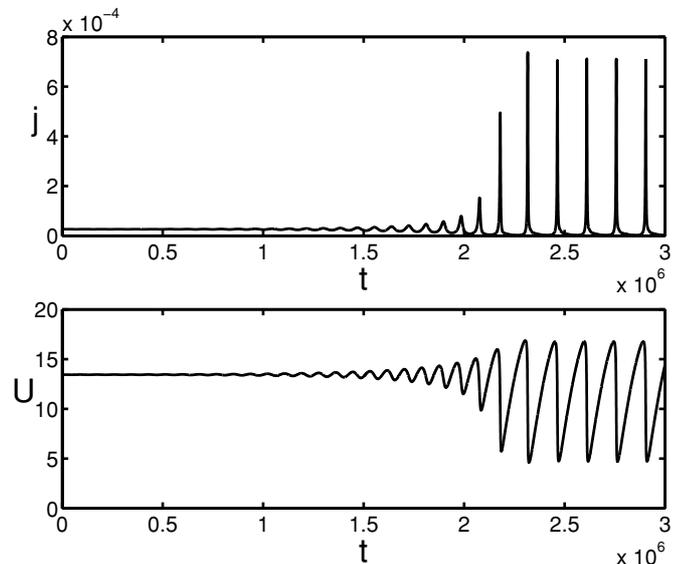
FIG. 5: $j(\tau)$ and $\mathcal{U}(\tau)$ for the parameters from (28), $\mathcal{R}_s = 4 \cdot 10^5$ and $\mathcal{U}_t = 24$. The stationary state now is linearly unstable and develops into a limit cycle.
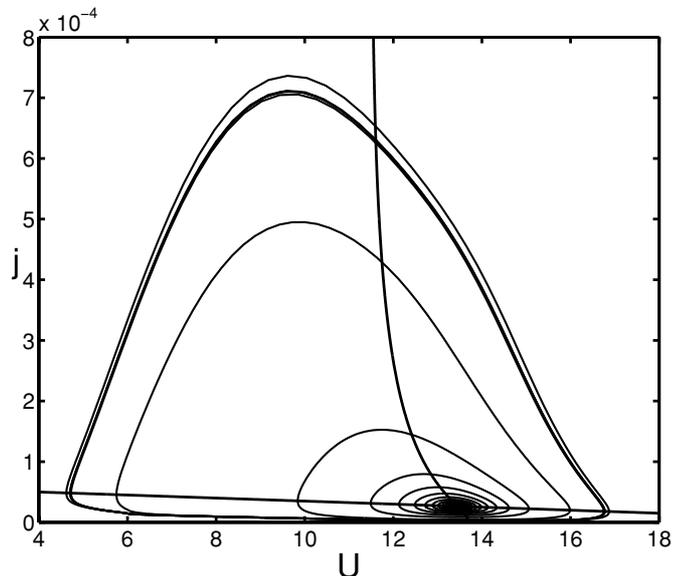
FIG. 6: Phase space plot of the data from Fig. 5 with current-voltage-characteristics and load line.

D. Quantitative comparison: amplitude and frequency of oscillations

The qualitative agreement of numerical solutions and experiment now encourages a more quantitative comparison. The thesis [11] contains diagrams on how frequency and maximal current amplitude depend on the semiconductor conductivity for a gas gap of 1 mm. It also contains the remark that frequency and amplitude for fixed conductivity depend in about the same way on the applied voltage as in the 0.5 mm gap of Ref. [10].

The same diagrams can also be derived from the numerically obtained limit cycle oscillations, they are presented in Fig. 7. The figure shows the current amplitude A and frequency f as a function of semiconductor conductance $1/\mathcal{R}_s$ for fixed voltage $\mathcal{U}_t$ or as a function of $\mathcal{U}_t$ for fixed $1/\mathcal{R}_s$.
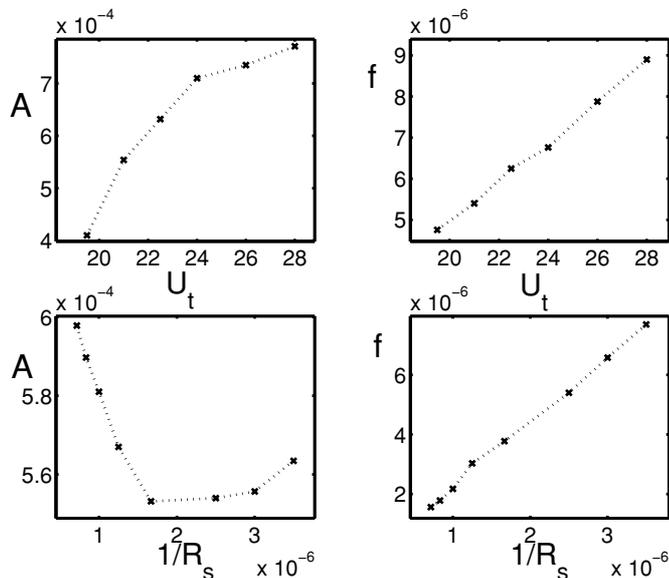
FIG. 7: Amplitude A and frequency f of the current oscillations as a function of applied total voltage $\mathcal{U}_t$ (for fixed resistance $R_s = 4 \cdot 10^5$) and as a function of conductivity $1/\mathcal{R}_s$ (for fixed voltage $\mathcal{U}_t = 21$).

We now compare the results. The upper left panel shows that the maximal current amplitude A as a function of applied voltage $\mathcal{U}_t$ is increasing with decreasing slope. This agrees with the statements written in [11]. The upper right panel shows that the frequency f is an almost linearly increasing function of applied voltage $\mathcal{U}_t$, this is actually in contradiction with the statement in [11] that the function would decrease.

The lower two panels allow a more quantitative comparison since corresponding experimental diagrams can be found in [11]. The experiments explore the range of $0.6 \cdot 10^{-7}/(\Omega\text{cm}) \leq \sigma_s \leq 2.8 \cdot 10^{-7}/(\Omega\text{cm})$ which corresponds to $0.62 \cdot 10^{-6} \leq 1/\mathcal{R}_s \leq 2.9 \cdot 10^{-6}$. The experimental diagrams for $U_t = 605$ V and 616 V in [11] show, that the amplitude A is very sensitive to this change while the

frequency f is rather robust. The numerical results are derived for $\mathcal{U}_t = 21$ which corresponds to $U_t = 600$ V.

In detail, the experimental curve for the current amplitude for 605 V shows first an increase from 0.2 to 0.8 mA with a subsequent sudden drop to essentially 0 from which the current suddenly jumps to values from 1.0 to 1.5 mA. For 616 V, in contrast, an almost continuous increase from 0.2 to 2.7 mA is observed for the same resistance range. Not too suprisinngly, our numerical results reproduce neither of these widely differing results at quite similar voltage. Rather, we observe an almost constant value in the range of $5.5 \cdot 10^{-4}$ to $6.0 \cdot 10^{-4}$ in the lower left pannel.

On the other hand, for the variation of the frequency f with conductivity, experiments [11] both for 605 V and for 616 V observe an about linear increase from 115 kHz or 125 kHz to 220 kHz ($4.6 \cdot 10^{-6} \leq f \leq 8.8 \cdot 10^{-6}$ in our dimensionless units) in the range of $0.62 \cdot 10^{-6} \leq 1/\mathcal{R}_s \leq 2.9 \cdot 10^{-6}$. Our numerical results in this range of $1/\mathcal{R}_s$ show the same linear increase, from $1.5 \cdot 10^{-6}$ to $6.5 \cdot 10^{-6}$. We believe that this agreement is quite convincing, in particular, since no parameter fitting was tried.

Summarizing, we find convincing agreement with experiment for A as function of $\mathcal{U}_t$ as well as for f as a function of $1/\mathcal{R}_s$. For the last, the available experimental results allow to identify an almost quantitative agreement. The sensitivity of the experimental results on A as a function of $1/\mathcal{R}_s$ does not allow quantitative comparison, and our results for f as a function of $\mathcal{U}_t$ deviate in their functional form from the available statements about experimental results.

E. Mechanism of the oscillations, reaction-diffusion models and surface charge

The voltage profiles $\mathcal{U}(\tau)$ in Figs. 2 and 5 show that there are two processes involved in the oscillations.

The first process occurs on the slow time scale τ_s of the semiconductor. It describes the exponential decay of the voltage $\mathcal{U}_t - \mathcal{U}(\tau) - \mathcal{R}_s j \propto e^{-\tau/\tau_s}$ over the semiconductor layer according to Eq. (23), as long as the contribution of $\mathcal{R}_s j$ does not vary substantially. The decay time τ_s is the Maxwell time due to resistance and capacitance of the semiconductor layer. τ_s accounts for the slow rise of the voltage $\mathcal{U}(\tau)$ over the gas discharge layer to a value above the current voltage characteristics of the gas discharge.

The other process is the electric breakdown of the gas discharge layer for sufficiently large $\mathcal{U}(\tau)$ which leads to a current pulse and a rapid subsequent decay of $\mathcal{U}(\tau)$.

It has been suggested by a number of authors [7, 15, 17, 32–37] that the current could be approximated by a similarly simple equation of the type $\partial_\tau j = g(\mathcal{U}, j)$, where g vanishes on the current-voltage-characteristics. This would bring the equations into a reaction diffusion form. However, as we already have discussed in [12], such an approximation of the underlying equations (18)–

(21), (25) and (26) is not possible, since it would not admit the period doubling events observed in [12], and it would not allow the phase space plots in Figs. 3, 4 and 6 to intersect the characteristics with a nonvanishing derivative, as they definitely do.

The physical reason for this behavior is the finite response time of the gas discharge layer, its "inertia" which doesn't allow an instantaneous reaction of the current. If ions are created by bulk impact ionization close to the anode, they will cross the whole gap until they reach the cathode and possibly liberate more electrons by secondary emission. The time that the ions need to cross the gap, is therefore an important scale of internal memory of the gas discharge. It can be approximated as $\tau_{ion} \approx L/(\mu\,\mathcal{E}) \approx L^2/(\mu\,\mathcal{U}(\tau))$ where $|\mathcal{E}|$ is some average field within the gas gap. For the gap of $L = 36$ ($d = 1$ mm), the ion crossing time is estimated as $2.6 \cdot 10^4$ for $\mathcal{U}(\tau) = 14$ or as $1.5 \cdot 10^4$ for $\mathcal{U}(\tau) = 24$ (which corresponds to 0.6 or 1 μs in dimensional units). This time is of the same order or larger than the duration of a current pulse, both in our numerical solutions and in the experimental results of Fig. 5 in [10]. (For the experiments on the 0.5 mm gap of Fig. 4 in [10], the situation seems to be different.)

Finally, it has been suggested in [38] that the surface charge on the interface between gas and semiconductor could play an important role, in a similar way as in AC discharges. This is certainly true, but the surface charge $q(\tau)$ is not an independent variable. Rather it is fully determined by the solution discussed above through

$$q(\tau) = \epsilon_s\,\frac{\mathcal{U}_t - \mathcal{U}(\tau)}{L} - \mathcal{E}(L,\tau). \qquad (35)$$

The assumption that this surface charge is the only relevant charge in the whole system doesn't lead to a satisfactory description either, but the space charges in the gas discharge layer have to be taken into account, too.

IV. STABILITY ANALYSIS: METHOD

The direct numerical solution of the dynamical problem is a time consuming procedure, that does not allow the exploration of a wide set of parameter values. We therefore have developed a linear stability analysis of the stationary state. It determines whether the stationary state is dynamically unstable and how small perturbations of such a state grow. In the present section, we present the method, and in the following one the results.

A. Problem setting and stationary solutions

The dynamical equations from section II.C are summarized as

$$\partial_\tau \sigma = \partial_z j_e + j_e \alpha(\mathcal{E}) \quad , \quad j_e = \sigma\mathcal{E}, \qquad (36)$$
$$\partial_\tau \mathcal{E} = j(\tau) - (1+\mu)j_e - \mu\mathcal{E}\partial_z\mathcal{E}, \qquad (37)$$

$$\tau_s \partial_\tau \mathcal{U}(\tau) = \mathcal{U}_t - \mathcal{U}(\tau) - \mathcal{R}_s j(\tau), \qquad (38)$$
$$0 = \partial_z \phi(z,\tau) + \mathcal{E}(z,\tau) \qquad (39)$$

with the boundary conditions

$$\partial_\tau \mathcal{E}(0,\tau) = j(\tau) - j_e(0,\tau), \qquad (40)$$
$$\partial_\tau \mathcal{E}(L,\tau) = j(\tau) - \frac{1+\gamma}{\gamma}j_e(L,\tau), \qquad (41)$$
$$\phi(L,\tau) = -\mathcal{U}(\tau) \quad , \quad \phi(0,\tau) = 0. \qquad (42)$$

The stationary solutions form the starting point of the perturbation analysis. They solve the equations

$$\partial_z j_{e0} = -j_{e0}\,\alpha(\mathcal{E}_0), \qquad (43)$$
$$\mu\mathcal{E}_0\,\partial_z\mathcal{E}_0 = j_0 - (1+\mu)j_{e0}, \qquad (44)$$
$$\partial_z \phi_0 = -\mathcal{E}_0, \qquad (45)$$
$$\mathcal{U}_0 = \mathcal{U}_t - \mathcal{R}_s j_0 \qquad (46)$$

with boundary conditions

$$j_{e0}(0) = j_0 \quad , \quad \frac{1+\gamma}{\gamma}\,j_{e0}(L) = j_0, \qquad (47)$$
$$\phi_0(0) = 0 \quad , \quad \phi_0(L) = -\mathcal{U}_0. \qquad (48)$$

Eqs. (43)–(45) with (47) and (48) define the current voltage characteristics $\mathcal{U} = \mathcal{U}(j)$ of a stationary discharge in the regime between Townsend and glow discharge [27, 28, 30]. Eq. (46) is the load line due to the external circuit. The intersection of load line and characteristics defines a generically discrete number of stationary solutions of the system as a whole.

B. Linear perturbations

For linear perturbations about this stationary state, we use the ansatz

$$j_e(z,\tau) = j_{e0}(z) + j_{e1}(z)\,e^{\lambda\tau}, \qquad (49)$$
$$\mathcal{E}(z,\tau) = \mathcal{E}_0(z) + \mathcal{E}_1(z)\,e^{\lambda\tau}, \qquad (50)$$
$$\phi(z,\tau) = \phi_0(z) + \phi_1(z)\,e^{\lambda\tau}, \qquad (51)$$
$$j(\tau) = j_0 + j_1\,e^{\lambda\tau}. \qquad (52)$$

The lower index 0 denotes the unperturbed stationary solutions while the lower index 1 denotes the linear perturbations about this stationary solution. The factorization of the perturbation into a z dependent function times the exponential $e^{s\tau}$ anticipates the eigenvalue problem of the solution.

In terms of the original variables, the explicit expansion in first order perturbation theory is a lengthy expression, but in terms of the variables

$$h = \frac{\sigma_1\mathcal{E}_0 + \sigma_0\mathcal{E}_1}{\sigma_0\mathcal{E}_0} = \frac{j_{e1}(z)\,e^{s\tau}}{j_{e0}(z)} \quad \text{and} \quad g = \mathcal{E}_0\,\mathcal{E}_1 \qquad (53)$$

the equations have a more compact form

$$\partial_z h = \frac{\lambda}{\mathcal{E}_0} h - \left(\frac{\alpha'(\mathcal{E}_0)}{\mathcal{E}_0} + \frac{\lambda}{\mathcal{E}_0^3} \right) g, \qquad (54)$$

$$\partial_z g = -(1+\mu) \frac{j_{e0}}{\mu} h - \frac{\lambda}{\mu \mathcal{E}_0} g + \frac{j_1}{\mu}, \qquad (55)$$

$$\partial_z j_1 = 0, \qquad (56)$$

$$\partial_z \phi_1 = -\frac{1}{\mathcal{E}_0} g \qquad (57)$$

with boundary conditions

$$\phi_1(0) = 0, \qquad (58)$$

$$j_1 = \frac{\lambda}{\mathcal{E}_0(0)} g(0) + j_0 \, h(0), \qquad (59)$$

$$j_1 = \frac{\lambda}{\mathcal{E}_0(L)} g(L) + j_0 \, h(L), \qquad (60)$$

$$\mathcal{R}_s j_1 = (1 + \lambda \tau_s) \, \phi_1(L). \qquad (61)$$

Here the equation $\partial_z j_1 = 0$ for the conservation of the total current is written explicitly in order to bring the equations into the homogeneous form

$$\partial_z \begin{pmatrix} h \\ g \\ j_1 \\ \phi_1 \end{pmatrix} = \begin{pmatrix} \frac{\lambda}{\mathcal{E}_0} & -\left(\frac{\alpha'}{\mathcal{E}_0} + \frac{\lambda}{\mathcal{E}_0^3}\right) & 0 & 0 \\ -\frac{1+\mu}{\mu} j_{e0} & -\frac{\lambda}{\mu \mathcal{E}_0} & \frac{1}{\mu} & 0 \\ 0 & 0 & 0 & 0 \\ 0 & -\frac{1}{\mathcal{E}_0} & 0 & 0 \end{pmatrix} \cdot \begin{pmatrix} h \\ g \\ j_1 \\ \phi_1 \end{pmatrix} \qquad (62)$$

The boundary conditions (58) and (59) at $z = 0$ can be written as orthogonality relations

$$\begin{pmatrix} j_0 \\ \frac{\lambda}{\mathcal{E}_0(0)} \\ -1 \\ 0 \end{pmatrix} \cdot \begin{pmatrix} h \\ g \\ j_1 \\ \phi_1 \end{pmatrix}_0 = 0 \quad , \quad \begin{pmatrix} 0 \\ 0 \\ 0 \\ 1 \end{pmatrix} \cdot \begin{pmatrix} h \\ g \\ j_1 \\ \phi_1 \end{pmatrix}_0 = 0. \qquad (63)$$

The general solution $\vec{v}(z)$ of (62) is therefore a superposition of two independent solutions $\vec{v}_1(z)$ and $\vec{v}_2(z)$ of (62) that both obey (63) in $z = 0$:

$$\vec{v}(z) = \begin{pmatrix} h(z) \\ g(z) \\ j_1(z) \\ \phi_1(z) \end{pmatrix} = C_1 \, \vec{v}_1(z) + C_2 \, \vec{v}_2(z). \qquad (64)$$

As initial conditions, one can choose, e.g.,

$$\vec{v}_1(0) = \begin{pmatrix} 1/j_0 \\ 0 \\ 1 \\ 0 \end{pmatrix} \quad , \quad \vec{v}_2(0) = \begin{pmatrix} 0 \\ \frac{\mathcal{E}_0(0)}{\lambda} \\ 1 \\ 0 \end{pmatrix}. \qquad (65)$$

The components of the two solutions are denoted as $\vec{v}_i(z) = \big(h_i(z), g_i(z), j_{1,i}(z), \phi_{1,i}(z) \big)$.

The boundary conditions (60) and (61) at $z = L$ also have the form of orthogonality relations

$$\begin{pmatrix} j_0 \\ \frac{\lambda}{\mathcal{E}_0(L)} \\ -1 \\ 0 \end{pmatrix} \cdot \begin{pmatrix} h \\ g \\ j_1 \\ \phi_1 \end{pmatrix}_L = 0 \quad , \quad \begin{pmatrix} 0 \\ 0 \\ -\mathcal{R}_s \\ 1 + \lambda \tau_s \end{pmatrix} \cdot \begin{pmatrix} h \\ g \\ j_1 \\ \phi_1 \end{pmatrix}_L = 0. \qquad (66)$$

Now each one of these two conditions determines the ratio C_1/C_2 of the general solution (64):

$$C_1 \left[j_0 h_1(L) + \frac{\lambda}{\mathcal{E}_0(L)} g_1(L) - j_{1,1}(L) \right]$$
$$+ C_2 \left[j_0 h_2(L) + \frac{\lambda}{\mathcal{E}_0(L)} g_2(L) - j_{1,2}(L) \right] = 0, \qquad (67)$$

$$C_1 \left[-\mathcal{R}_s j_{1,1}(L) + (1 + \lambda \tau_s) \phi_{1,1}(L) \right]$$
$$+ C_2 \left[-\mathcal{R}_s j_{1,2}(L) + (1 + \lambda \tau_s) \phi_{1,2}(L) \right] = 0, \qquad (68)$$

where $j_{1,1}(L) = 1 = j_{1,2}(L)$, since these components have this value at $z = 0$ according to (65): $j_{1,1}(0) = 1 = j_{1,2}(0)$, and since the equation of motion for j_1 is $\partial_z j_1 = 0$. A nontrivial solution of both (67) and (68) requires the determinant

$$\Delta = \qquad (69)$$
$$\begin{vmatrix} j_0 h_1(L) + \frac{\lambda}{\mathcal{E}_0(L)} g_1(L) - 1 & j_0 h_2(L) + \frac{\lambda}{\mathcal{E}_0(L)} g_2(L) - 1 \\ -\mathcal{R}_s + (1 + \lambda \tau_s) \phi_{1,1}(L) & -\mathcal{R}_s + (1 + \lambda \tau_s) \phi_{1,2}(L) \end{vmatrix}$$

to vanish. This condition leads to a quadratic equation for the eigenvalue λ.

C. Rescaling with μ and numerical calculation

The eigenvalue λ can now be calculated numerically.

First, it should be noted, that the equation of motion (62) has matrix elements of very different size, since μ is a very small parameter. However, this apparent stiffness of the problem can be removed by introducing the new parameters

$$\iota_e = \frac{j_e}{\mu} \quad , \quad \iota = \frac{j}{\mu} \quad , \quad r_s = \mathcal{R}_s \mu, \qquad (70)$$

$$\bar{\tau}_s = \tau_s \mu \quad , \quad s = \frac{\lambda}{\mu}.$$

The introduction of rescaled current density and time scale and resistivity has a direct physical motivation. Previous analysis of the stationary solutions [27, 28, 30] as well as the dynamical solutions of Section III and [12] show that velocities should actually be measured on the time scale of the ions and not of the electrons. So the time scale should be measured in units of $t_+ = 1/(\alpha_0 \mu_+ E_0) = t_0/\mu$ rather than in units of $t_0 = 1/(\alpha_0 \mu_e E_0)$. The rescaling (70) directly follows from this consideration.

Now the eigenvalue s can be calculated numerically as follows: First an initial estimate s_0 is chosen. Then the two initial conditions (65) at $z = 0$ are integrated numerically with (62) up to $z = L$. Generically, the determinant Δ (69) will then be non-vanishing. The request that the determinant does vanish, fixes a new value for s that is used for the next step of the iteration within an under-relaxation method that garantuees the stability of the convergence. This procedure is repeated until an accuracy of

$$\left| \frac{s_{k+1} - s_k}{s_{k+1}} \right| < 10^{-6} \qquad (71)$$

is reached.

The eigenvalue s is in general a complex parameter whose real part describes the growth or decay of the oscillation amplitude while its imaginary part describes the oscillation frequency. Since s is a parameter in the equation of motion (62), also the vector $\vec{v}(z)$ has complex entries. Therefore 16 real functions Re $h_1(z)$, Im $h_1(z)$ etc. have to be integrated over z. It is convenient to also integrate the two real functions j_{e0} and $\mathcal{E}_0$ that enter the matrix (62) together with the perturbations. The iteration program is written in fortran 90 with complex variables. For the integration of equations, a 4th order Runge-Kutta method is used. The number of grid points used was 500, since 1000 or 2000 grid points give essentially the same result.

V. STABILITY ANALYSIS: RESULTS

In the present section, the validity of the stability analysis results are confirmed by comparison with numerical solutions of the full dynamical problem. The stability analysis is then used to determine the phase diagram for the onset of oscillating solutions. These phase diagrams are then compared with experimental results, again with semi-quantitative agreement.

A. The structure of the results

The stability analysis determines not only the complex eigenvalue λ, but also the whole linear correction

$$\vec{v}(z) = C_1 \left[\vec{v}_1(z) - \frac{\mathcal{R}_s + (1 + \lambda\tau_s)\,\mathcal{U}_{1,2}(L)}{\mathcal{R}_s + (1 + \lambda\tau_s)\,\mathcal{U}_{1,1}(L)}\,\vec{v}_2(z) \right],$$
(72)

up to the arbitrary complex constant C_1.

This $\vec{v}(z)$ determines the evolution of current and voltage in linear approximation about the stationary solution $(j_0, \mathcal{U}_0)$:

$$j(\tau) = j_0 + j_1\,e^{\lambda\tau} + c.c., \tag{73}$$
$$\mathcal{U}(\tau) = \mathcal{U}_0 + \mathcal{U}_1\,e^{\lambda\tau} + c.c., \tag{74}$$

where c.c. denotes the complex conjugate. The ratio between $\mathcal{U}_1$ and j_1 is fixed through the boundary condition (61) to the value

$$\mathcal{U}_1 = -\frac{j_1}{(1 + \lambda\tau_s)/\mathcal{R}_s} = r\,e^{i\alpha}\,j_1, \tag{75}$$

where
$$r = \frac{\mathcal{R}_s}{|1 + \lambda\tau_s|} \quad \text{and} \tag{76}$$

$$\cos\alpha = -\frac{1 + \text{Re}\,\lambda\tau_s}{|1 + \lambda\tau_s|} \quad,\quad \sin\alpha = \frac{\text{Im}\,\lambda\tau_s}{|1 + \lambda\tau_s|}.$$

The final result is

$$j(\tau) = j_0 + c\,\mu\,e^{\text{Re}\,\lambda\tau}\,\cos(\text{Im}\,\lambda\tau + \alpha_0)\,, \tag{77}$$
$$\mathcal{U}(\tau) = \mathcal{U}_0 - c\,r\,e^{\text{Re}\,\lambda\tau}\,\cos(\text{Im}\,\lambda\tau + \alpha + \alpha_0) \tag{78}$$

where amplitude c and absolute phase α_0 reflect the arbitrary factor C_1 in (72) and are adjustable while all other parameters are fixed.

B. Comparison with solutions of the full PDE's

As a check of accuracy, these solutions are now first compared with numerical solutions of the full PDE problem.

For the set of parameters from Figs. 2, 3 and 4, the stationary solution is $(j_0, \mathcal{U}_0) = (1.49 \cdot 10^{-5}, 13.583)$, and the eigenvalue λ has the complex value $\lambda = -2.913 \cdot 10^{-6} \pm i\,4.822 \cdot 10^{-5}$. As $\tau_s = 340/\mu$ and $\mathcal{R}_s = 1400/\mu$, the ratio of current and voltage amplitude $r = 295/\mu$ and the phase shift $\alpha = 98.69^o$ are determined through Eq. (76).

The comparison of these predictions from the stability analysis with numerical solutions of the full PDE problem are shown in Fig. 8. Here the free parameters for the total amplitude c and the absolute phase α_0 were chosen such as to fit the PDE-data well.
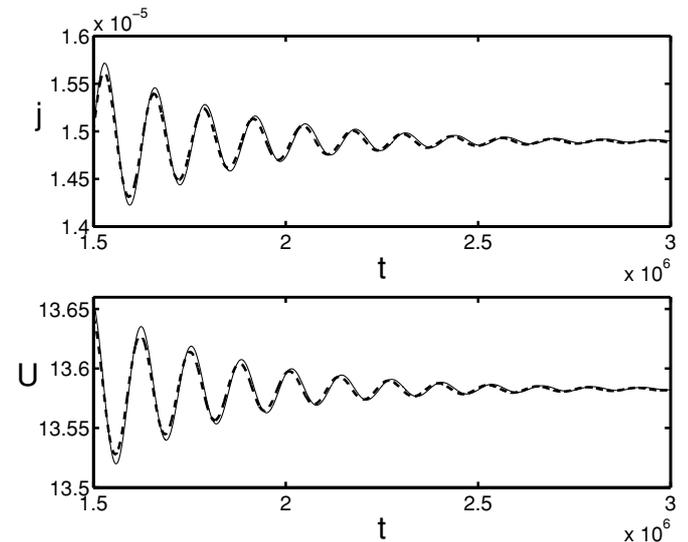
FIG. 8: Comparison of $j(\tau)$ and $\mathcal{U}(\tau)$ from the stability analysis (solid lines) with the result from the simulation (dashed lines) for the parameter values of Figs. 2-4.

This visual agreement can be tested in more detail. In particular, we used the PDE-data in the time interval $5 \cdot 10^5 < \tau < 6.5 \cdot 10^5$ to determine the phase shift α between $\mathcal{U}_1$ and j_1. It is $\alpha = (100 \pm 0.4)^o$, convincingly close to the predicted value of $\alpha = 98.69^o$.

Increasing the total applied voltage $\mathcal{U}_t$, the real part of the eigenvalue λ grows until it becomes positive. This means that the stationary solution becomes linearly unstable and perturbations will grow. An example of such behavior occurs for $\mathcal{U}_t = 24$ with all other parameters as before. The stationary solution is

then $(j_0, \mathcal{U}_0) = (2.64 \cdot 10^{-5}, 13.441)$, the eigenvalue is $\lambda = 2.493 \cdot 10^{-6} \pm i\, 7.375 \cdot 10^{-5}$, the ratio of current and voltage amplitude is $r = 192/\mu$ and the phase shift is $\alpha = 99.83^o$.

Fig. 9 shows again the comparison between these results and the numerical solutions of the full PDE's. Again, the agreement is very convincing.
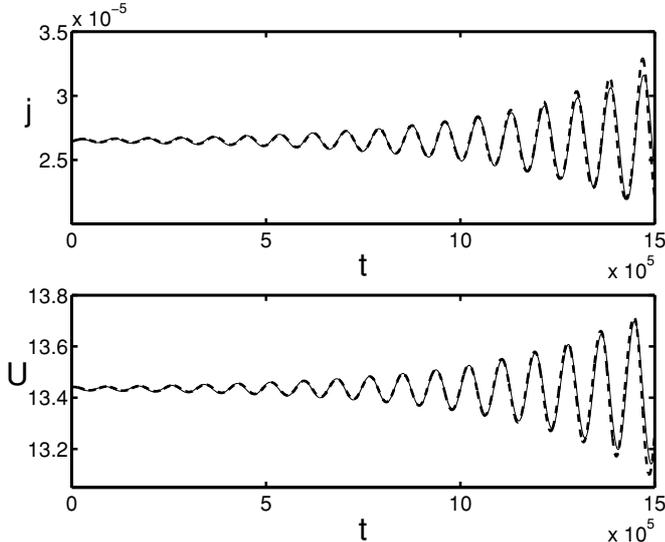
FIG. 9: Comparison of $j(\tau)$ and $\mathcal{U}(\tau)$) from the stability analysis (solid lines) with the result from the simulation (dashed lines) for the parameter values of Figs. 5-6 where the stationary solution is unstable.

Of course, the predictive power of linear stability analysis is limited to small perturbations with $j_1 \ll j_0$ and $\mathcal{U}_1 \ll \mathcal{U}_0$. When the amplitude of the oscillation from Fig. 6 increases further, nonlinear couplings set in and the system finally reaches a limit cycle as shown in Fig. 7.

C.   Calculation of phase diagrams

The stability analysis now allows one to derive the bifurcation line where a homogeneous stationary state looses its stability. Fig. 10 shows this bifurcation line for the parameters (28) as a function of applied voltage $\mathcal{U}_t$ and conductivity $1/\mathcal{R}_s$ for three different values of γ. Besides the value $\gamma = 0.08$ used everywhere else in the paper, also results for $\gamma = 0.04$ and 0.16 are shown to illustrate the sensitivity of theoretical predictions to this parameter. For Re $\lambda < 0$, the stationary state is linearly stable, while for Re $\lambda > 0$, the system is always in the oscillating state.

Comparison with the experimental phase diagram in Fig. 11 for the gas gap with a corresponding width of $d = 1$ mm [11, 39] shows qualitative and quantitative correspondences, but also deviations. Experiments in the 1 mm gap for $U_t < 585$ V ($\mathcal{U}_t = 20.5$) do not exhibit oscillations. The same holds theoretically for a secondary
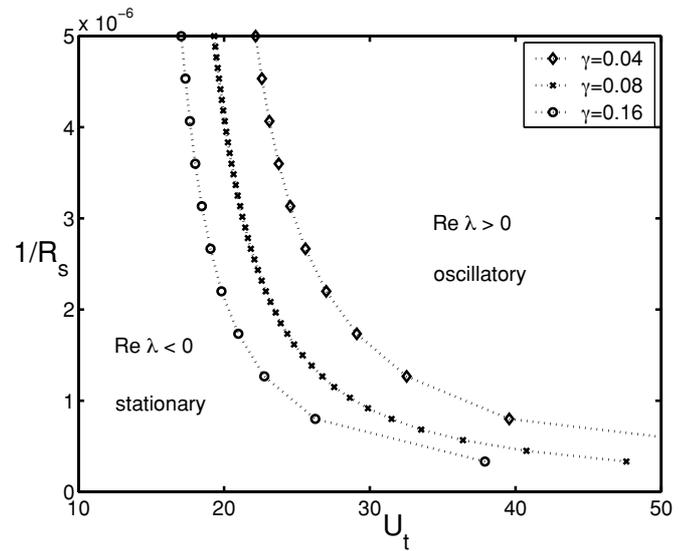
FIG. 10: Bifurcation diagram for the parameters from (28) (where $L = 36$) and 3 different values of γ. The lines separate regions with Re $\lambda < 0$ where the stationary state is linearly stable from regions with Re $\lambda > 0$ where the homogeneous stationary state looses its stability.
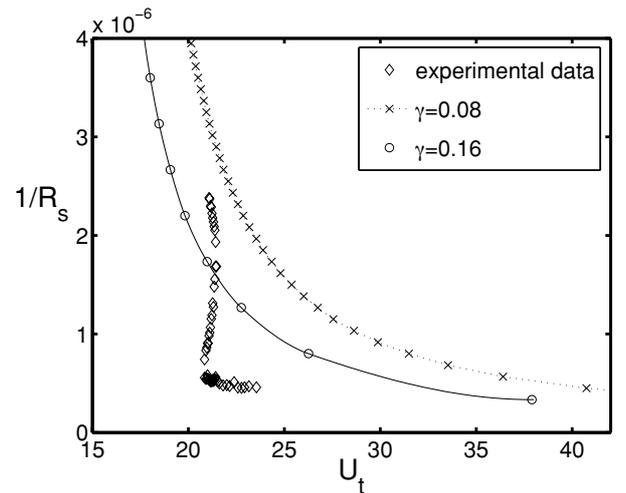
FIG. 11: Blow up of the bifurcation diagram in Fig. 10 for two different values of γ and comparison with experimental data [11, 39]. Theoretical lines and experimental lines are in same region of parameters and have same limits.

emission coefficient of 0.08 or smaller. In detail, experiments show that the raising phase transition line initially raises with positive slope then changes gradually to being almost parallel to the σ_s axis and then continues with negative slope up to the maximal experimentally reached σ_s.

For the low conductivity of the semiconductor layer, the experiment shows another bifurcation line almost parallel to the U_t axis at values of σ_s around $0.5\,\cdot$

$10^{-7}/(\Omega \text{ cm})$. In dimensionless units this corresponds to a plateau at values of $1/\mathcal{R}_s$ around $0.5 \cdot 10^{-6}$. An approach to such a plateau can also be seen in the calculated phase diagram. However, the theoretical curve crosses over continuously to this plateau, while the experimental curve seems to show the intersection of two bifurcation lines with quite distinct slope. We have no explanation for this deviation.

It is remarkable that the bifurcation theory also covers the almost horizontal bifurcation line for small $1/\mathcal{R}_s$. Another explanation for this experimentally observed feature of the phase diagram would have been a breakdown of the continuum approximation: the recovery phase of the oscillation would have carried such a low current that the discreteness of the electrons would have to be taken into account.

Finally, it was observed experimentally [10, 11] that increasing the system size L while keeping other conditions unchanged, the frequency decreases and oscillations set in at higher voltages. This agrees with our calculated phase diagram in Fig. 11. Indeed, for $\mathcal{U}_t < 22.5$, the homogeneous stationary state is stable for $L = 72$.
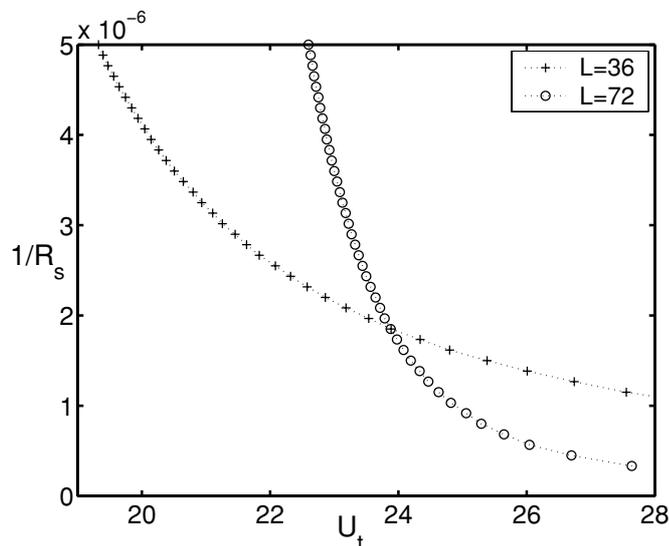
FIG. 12: Bifurcation diagram for $\gamma = 0.08$, $L = 36$ and $L = 72$.

VI. CONCLUSION

We have analyzed the simplest model for a one-dimensional short gas discharge coupled to an external circuit with resistor, capacitance and stationary voltage. This analysis is directly applicable to experiments performed in [10, 11].

We have presented fully numerical solutions as well as a linear stability analysis of the stationary state of the system which are in very good mutual agreement. The numerical solutions reproduce experimental observations of bistability and oscillations in a semi-quantitative manner, though the model is minimal and no attempt of parameter fitting has been made. The stability analysis allows us to derive bifurcation diagrams in a simple manner, they also agree overall with experimentally obtained bifurcation diagrams.

It should be remarked that we have constrained the analysis to the gap of 1 mm wide; the gap of 0.5 mm is so sensitive to the actual value of secondary emission γ that quantitative analysis based on a fixed value of γ seemed doubtful.

We have reproduced a number of experimental observations up to the dependence of oscillation amplitude on applied potential and of the oscillation frequency on the conductivity of the semiconductor layer, while discrepancies of other observables will stay a subject of investigation. This opens up the way to investigate now the spatial and spatio-temporal patterns in the next step.

[1] B. Bruhn, B.-P. Koch, and P. Jonas, Phys. Rev. E **58**, 3793 (1998).

[2] B. Bruhn and B.-P. Koch, Phys. Rev. E **61**, 3078 (2000).

[3] Yu.B. Golubovski, V.A. Maiorov, V.O. Nekutchaev, J. Behnke and J.F. Behnke, Phys. Rev. E **63**, 036409 (2001).

[4] C. Letellier, A. Dinklage, H. El-Naggar, C. Wilke and G. Bonhomme, Phys. Rev. E **63**, 042702 (2001).

[5] A. Bultel, C. Letellier and A. Bourdon, Phys. Lett. A **323**, 267 (2004).

[6] W. Breazeal, K.M. Flynn, E.G. Gwinn, Phys. Rev. E **52**,

1503 (1995).

[7] R.Sh. Islamov, Phys. Rev. E **64**, 046405 (2001).

[8] L. Dong et al., Thin Solid Films **435**, 120 (2003).

[9] S. Nasuno, Chaos **13**, 1010 (2003).

[10] C. Strümpel, Y.A. Astrov, H.-G. Purwins, Phys. Rev. E **62**, 4889 (2000).

[11] C. Strümpel, Ph.D. thesis, Univ. Münster, Germany, 2001.

[12] D.D. Šijačić, U. Ebert, I. Rafatov, Phys. Rev. E **70**, 056220 (2004).

[13] Z.Lj. Petrović and A.V. Phelps, Phys. Rev. E **47**, 2806

(1993).

[14] B.M. Jelenković, K. Rózsa, and A.V. Phelps, Phys. Rev. E **47**, 2816 (1993).

[15] A.V. Phelps, Z.Lj. Petrović and B.M. Jelenković, Phys. Rev. E **47**, 2825 (1993).

[16] Z.Lj. Petrović, A.V. Phelps, Phys. Rev. E **56**, 5920 (1997).

[17] V.I. Kolobov and A. Fiala, Phys. Rev. E **50**, 3018 (1994).

[18] I. Pérès, L.C. Pitchford, J. Appl. Phys. **78**, 774 (1995).

[19] L.M. Portsel, Y.A. Astrov, I. Reimann, H.-G. Purwins, J. Appl. Phys. **81**, 1077 (1997).

[20] R.R. Arslanbekov, V.I. Kolobov, J. Phys. D **36**, 2986 (2003).

[21] T. Braun et al., Phys. Rev. Lett. **59**, 613 (1987).

[22] J. Qin et al., Phys. Rev. Lett. **63**, 163 (1989)

[23] P.Y. Cheung, S. Donovan, and A.Y. Wong. Phys. Rev. Lett. **61** (12), 1360 (1988).

[24] V.O. Papanyan and Yu.I. Grigoryan. Physics Letters A **164**, 43 (1992).

[25] Ranjit Singh, P.S.R. Prasad, J.K. Bhattacharjee, and R.K. Thareja. Physics Letters A **178**, 284 (1993).

[26] P.R. Sasi Kumar, V.P.N. Nampoori, and C.P.G. Vallabhan. Physics Letters A **196**, 191 (1994).

[27] D.D. Šijačić, U. Ebert, Phys. Rev. E **66**, 66410 (2002).

[28] Yu.P. Raizer, U. Ebert, D.D. Šijačić, Phys. Rev. E **70**, 017401 (2004).

[29] U. Ebert, W. van Saarloos, C. Caroli, Phys. Rev. E **55**, 1530 (1997).

[30] Yu.P. Raizer, *Gas Discharge Physics* (Springer, Berlin, 1991).

[31] M. Surendra, D.B. Graves, L.S. Plano, J. Appl. Phys. **71**, 5189 (1992).

[32] K.G. Müller, Phys. Rev. A **37**, 4836 (1988).

[33] H.-G. Purwins *et al.*, Phys. Lett. A **136**, 480 (1989).

[34] C. Radehaus *et al.*, Phys. Rev. A **42**, 7426 (1990).

[35] C. Radehaus *et al.*, Phys. Rev. A **45**, 2546 (1992).

[36] Z.L. Petrovic, I. Stefanovic, S. Vrhovac, and J. Zivkovic, J. Phys. IV France **7**, Colloque C4, 341-352 (1997).

[37] Yu.A. Astrov, Y.A. Logvin, Phys. Rev. Lett. **79**, 2983 (1997).

[38] E.L. Gurevich, A.W. Liehr, Sh. Amiranashvili, and H.-G. Purwins, Phys. Rev. E **69**, 036211 (2004).

[39] D. Šijačić, Ph.D. thesis, Technical University Eindhoven, The Netherlands, 2004. ISBN 90-386-2035-7 http://alexandria.tue.nl/extra2/200413150.pdf